J Mater Sci (2023) 58:4115–4136

Materials for life sciences

Mechanical, corrosion, and tribocorrosion behavior of biomedical ZrO_2 ceramic coatings prepared by thermal oxidation

F. Sourani[1,*], K. Raeissi[1], M. H. Enayati[1], Paul K. Chu[2], and H. R. SalimiJazi[1]

[1] *Department of Materials Engineering, Isfahan University of Technology, Isfahan 84156-83111, Iran*
[2] *Department of Physics, Department of Materials Science and Engineering, Department of Biomedical Engineering, City University of Hong Kong, Tat Chee Avenue, Kowloon, Hong Kong, China*

Received: 30 September 2022
Accepted: 16 January 2023
Published online:
22 February 2023

ABSTRACT

For the simultaneous improvement of mechanical, corrosion, and tribo-corrosion properties of Zr–2.5Nb alloy, an adherent black coating was deposited on the Zr–2.5Nb substrate by thermal oxidation in air at different temperatures and times to use in biomedical applications such as knee joints and orthopedic/dental replacements. According to obtained results, the long-term corrosion and tribo-corrosion resistance, and frictional properties in the phosphate-buffered saline solution improved significantly by oxidization at 523 °C for 4 h compared to the bare substrate. XRD patterns and Raman spectra revealed the formation of monoclinic and tetragonal ZrO_2, as well as Nb_2O_5 phases in the black coating. According to microstructural studies, high adherence between the compact oxide layer and substrate decreased due to the formation of micro-cracks in the coating at a high operating temperature of 700 °C.

Handling Editor: Maude Jimenez.

Address correspondence to E-mail: f.sourani@alumni.iut.ac.ir

https://doi.org/10.1007/s10853-023-08211-1

GRAPHICAL ABSTRACT

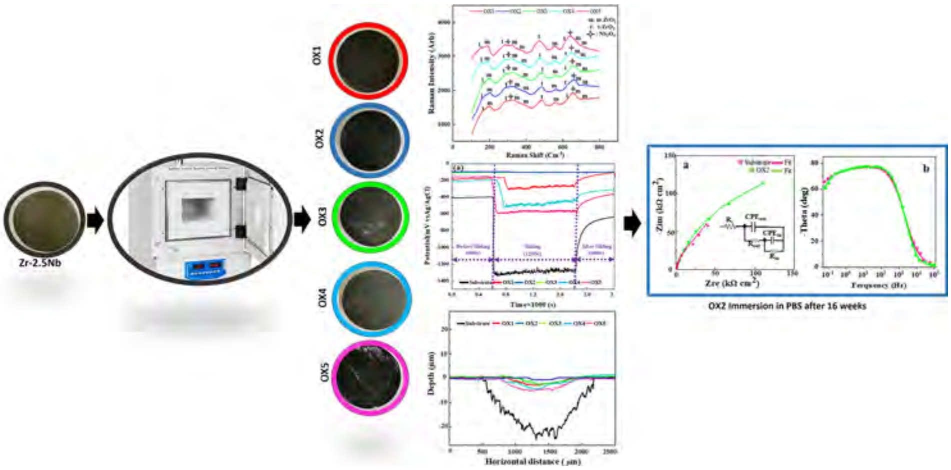

Introduction

During end-stage arthritis, total knee arthroplasty (TKA) is often the reliable and effective method to restore joint functions [1–4]. Total knee implants must possess high strength, corrosion and wear resistance, tissue compatibility, longevity, and low friction coefficients. Zr and Zr-alloys are commonly used in biomedical implants, prosthetic components, and dental prostheses due to their high fracture toughness, strength, wear resistance, and good biocompatibility [5–9] in comparison with other common biomedical materials including CoCrMo alloys, Ti-6Al-4 V, and 316L stainless steel [10, 11]. Moreover, the zirconium dioxide (ZrO_2) ceramic surface has enhanced hemocompatibility [12].

Oxide ceramic materials offer benefits as articulating surfaces on TKA and hemiarthroplasty devices due to their good wear resistance and high lubricity, but there are some drawbacks including the brittle nature and difficulty to fabricate implants with the required shape and topography. Therefore, coupling ceramic materials with mechanically resilient metallic substrates offer some advantages. The oxidized zirconium (OxZr) alloy with the trade name OXINIUM utilizes oxidation to transform the metallic surface into a ceramic one. Zirconia (ZrO_2) has been used as a coating on metallic substrates to enhance cell adhesion and proliferation while providing abrasion and wear resistance [13]. It has three well-known crystallographic structures. The structural studies of zirconia have shown that it is polymorphous and exists in three crystallographic phases: (i) monoclinic (m), lowest symmetry structure with thermodynamically stable up to 1170 °C; (ii) tetragonal (t), appears from 1170 to 2370 °C; and (iii) cubic (c), from 2370 to 2715 °C (melting temperature). Under these changes in symmetry, its physicochemical properties get improved, which means that high-temperature phases are extra suitable for industrial applications [7]. The transition from one structure to another occurs with martensitic transformation which often leads to crack formation. Therefore, various strategies have been proposed to mitigate cracking in ZrO_2-based ceramics [14], and the stability of two phases including tetragonal (t-ZrO_2) and monoclinic (m-ZrO_2) is the main concern. The transformation from t-ZrO_2 to m-ZrO_2 is accompanied by 3% volume expansion which prevents crack progression[15]. Ling et al. [16] reported that the martensitic transformation temperature of zirconia from m–ZrO_2 to t–ZrO_2 during the heating stage was reduced under the radiation of microwave energy. The increase in heating temperature was useful for the transformation of monoclinic phase zirconia to tetragonal phase zirconia, thus increasing the stability rate of partially stabilized zirconia. The optimized sintering effect appears at 1000 °C in the studied roasting temperature range (800–1200 °C) for Al_2O_3–ZrO_2 powders [17].

One of the important requirements for joint materials used in joint arthroplasty is to survive sliding under large localized loads. Therefore, it is essential to investigate the corrosion and tribocorrosion resistance of joint replacement alloys under physiological conditions. Several tribological studies conducted in vitro and in vivo have revealed the superiority of ceramics in wear applications, especially articulating against polyethylene in comparison with metallic components due to the reduced amount of UHMWPE debris [2].

Amat et al. [18] have shown that the mechanical properties of ZrO_2 are influenced by the microstructure and also processing conditions. Denry et al. have demonstrated that a microstructure with finer grains, high homogeneity, and low porosity has better mechanical properties. Ezzet et al. [19] have reported a nearly 50% decline in the wear rates after 5 million cycles and ZrO_2 can withstand up to 50 billion cycles without breaking at an applied force of up to 90 kN in comparison with the failure of other biomaterials in 15 cycles [20]. Gautam et al. [20] have observed no spalling or delamination of zirconia-coated zirconium alloy even after 10 million abrasion cycles. It is assumed that the roughness of the surface also influences the wear because a smoother surface decreases friction and enhances lubrication. The effects of the Nb content on the microstructure and corrosion resistance of biomedical Zr–Nb alloys have been investigated by Zhou et al. [21]. Early clinical trials have also disclosed favorable results for oxidized zirconium as well as the possibility of improving the durability of total hips and knee arthroplasty by this alloy [22].

Various methods have been employed clinically to treat Zr-alloy-based total hip and knee replacements [2]. An oxidation process has been proposed for orthopedic Zr alloy implants, in which the load-bearing surface is covered by a dense and thin layer of black-zirconium or blue-black-zirconium oxide [15, 23]. Internal oxygen diffusion results in the formation of a dense-protective black oxide layer with a thickness of about 5 μm due to good conduction of ZrO_2 and a porous surface with insufficient protection is produced at a longer oxidation time, thereby degrading the corrosion and wear resistance against bone cement and oxide debris, while lower sliding friction against polyethylene at the same time [24]. In the present study, thermal oxidation in air at different temperatures and times was designed to obtain the adherent-black coatings on the Zr–2.5Nb alloy. The main objective of this work is to comprehensively investigate the corrosion and tribocorrosion performance of the black coatings in the phosphate-buffered saline solution (PBS). The results represented a significant improvement in corrosion and tribocorrosion resistance values by increasing the oxidation temperature to 523 °C due to the formation of ZrO_2–Nb_2O_5 ceramic coatings on Zr–2.5Nb substrate which makes them an interesting candidate for substituting metallic implants which exhibit weak to moderate corrosion and tribocorrosion resistance, especially for biomedical applications such as knee joints.

Experimental details

Thermal oxidation

Commercial disk-shaped (20 mm in diameter × 5 mm thick) Zr–2.5Nb alloy with the chemical composition (%wt.) of Nb: 2.64, Fe: 0.011, other impurities < 0.01, and Zr: remainder, was used as the substrate. The Zr–2.5Nb alloy density and average porosity percent were about 6.5 $gr.cc^{-1}$ and $< 1\%$, respectively. The specimens were ground with silicon carbide paper of 600, 1200, 2500, and 4000 grits and finally polished with alumina and 0.5 μm diamond paste to produce a smooth surface. They were cleaned ultrasonically in distilled water and alcohol. Thermal oxidation was performed in an electrical muffle furnace (MET.F1200) in the air at 523 °C for 3, 4, and 5 h and 700 and 800 °C for 1 h. The specimens were oxidized before cooling to room temperature in each cycle. The label of the specimens according to the oxidation time and temperature is shown in Table 1. Figure 1 represents the macroscopic image of the oxidized specimens after removal from the furnace.

Table 1 Label of the specimens

Specimen label	OX1	OX2	OX3	OX4	OX5
Temperature (°C)	523	523	523	700	800
Time (h)	3	4	5	1	1

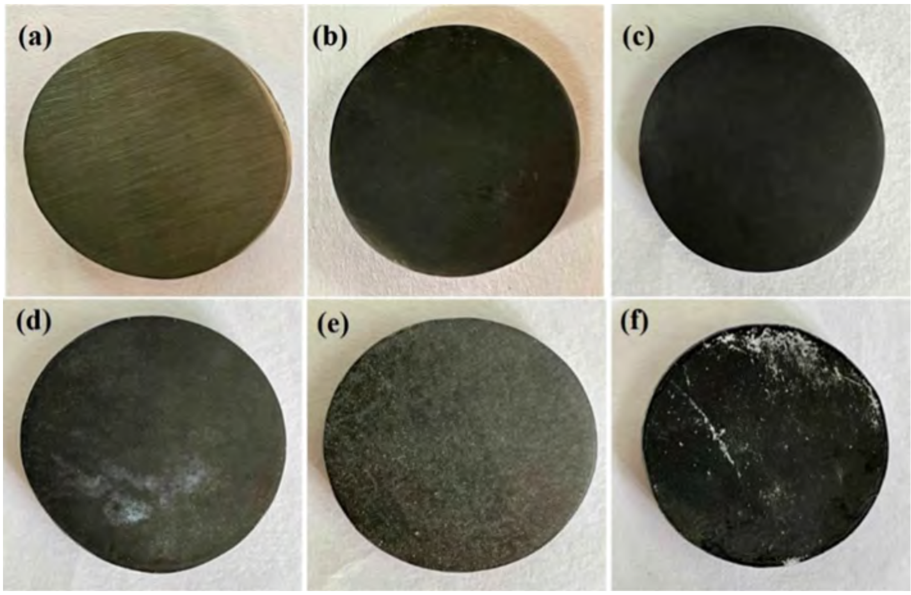

Figure 1 Macroscopic images of the oxidized specimens: **a** Zr-2.5Nb alloy, **b** OX1, **c** OX2, **d** OX3, **e** OX4, and **f** OX5.

Characterization of the oxidized specimens

The phase composition was detected by X-ray diffraction (XRD, model PANalytical), using Cu K_α radiation (40 kV and 40 mA) for the 2θ range of 10–80°, 0.05° step size, and 1 s step time. The X'Pert high score software (version 3.0.0) with the PDF2 database was used to analyze the XRD patterns. Scherrer's equation [25] was used to determine the average crystallite size of ZrO_2 phases by utilizing the width of XRD peaks at half maximum intensity (β), the diffraction angle (θ), and the X-ray wavelength (λ):

$$\mathrm{d(nm)} = \frac{0.9\lambda}{\beta\cos\theta} \quad (1)$$

In addition, micro Raman scattering was carried out using the Nd:YAG laser with a wavelength of 532 nm on the Renishaw inVia Raman Microscope equipped with a (50x) microprobe and a CCD detector to determine the functional groups and vibrations caused by different phases present in the oxide coatings on the surface of the Zr–2.5Nb alloy. A scanning electron microscope (SEM, model LEO 1530) equipped with the Oxford X-Max energy-dispersive X-ray spectrometer (EDS) and field-emission scanning electron microscope (FE–SEM) were used to examine the cross section and surface morphology of the coatings. The cross sections were prepared by mounting the samples vertically in epoxy resin and mechanically grinding near parallel to the coating/substrate interface direction using emery paper down to 2400 grit. After that, the samples were polished using alumina particles.

(1 micron) and then washed using double distilled water and methanol, and finally dried in warm airflow. The gold spattering was applied to cover the mounted samples before placing them in the SEM chamber. The average oxide layer thickness was determined by the ImageJ 1.44p software on the cross section of SEM micrographs, and the surface roughness (R_a) was monitored by profilometry (model Mitutoyo SJ210). The relative density of the oxidized specimen was measured using the immersion technique as specified in ASTMB311 and the relative density was reported as the ratio of the measured density to the theoretical density.

Surface hardness

The mechanical properties were investigated on both the nano- and micro-scales. The nano-hardness test was performed on the Agilent Nanoindenter equipped with a Berkovich tip and XP transducer with unmatched flexibility for the 40 mN load. The nanoindentation tests were carried out on a 5 × 5 array and were repeated 10 times for every region of each sample. The maximum depth was set to 2000 nm, with a holding time of 10 s before unloading. To calculate the nano-hardness value and the elastic modulus of the coating, common load–displacement diagrams with the Berkovich standard diamond indenter were employed and plotted automatically during each test. The average micro-

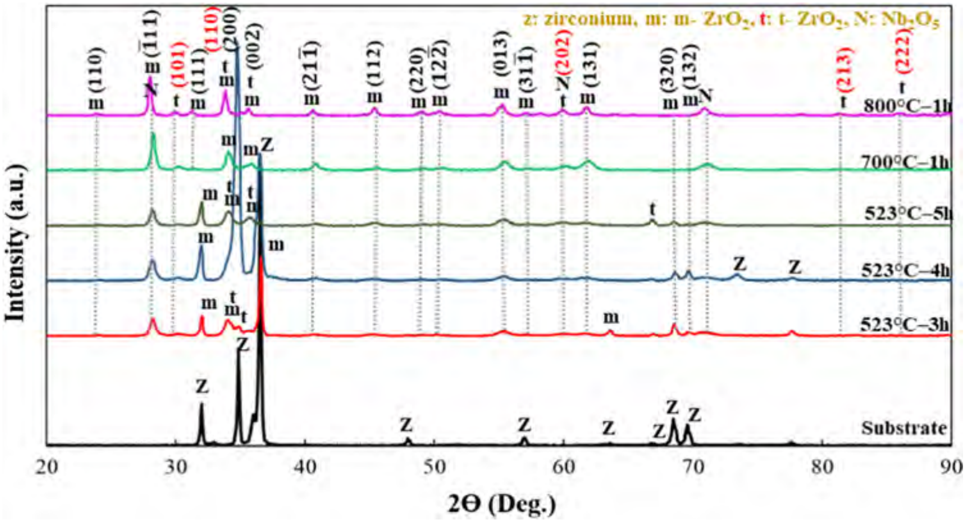

Figure 2 X-ray diffraction patterns of the Zr-2.5Nb substrate and oxide coatings formed at different temperatures at different times.

hardness was measured on the cross section of the coatings by a diamond Knoop indenter at a load of 25 g, which is more suitable for thin coatings (five indents at the center of each specimen).

To investigate the H and E profiles along the region of oxidation, three batches of seven indentations were performed in all the coatings from the interface to the outer layer. The tests were performed with an advance of 2 µm and lateral displacement of 7 µm related to the last indentation.

Corrosion properties

The electrochemical properties of the oxide layers were evaluated by electrochemical impedance spectroscopy (EIS) in the phosphate-buffered saline (PBS) solution (Na^+: 138.7, K^+: 3.1, Cl^-: 139.7 and HPO_4^{-2}: 2.03 mmol. L^{-1}) on the AMETEK potentiostat/galvanostat (model PARSTAT 2273) (Tennessee, USA) at 37 °C based on the three-electrode cell in which the platinum plate was the counter electrode, saturated Ag/AgCl as the reference electrode, and one face of the coated sample of 1 cm^3 area (working electrode) was exposed to the aggressive electrolyte. The Power Suite software was used to analyze the data. For evaluating the stability of the coatings, the EIS measurements were continued for long immersion times using duplicate samples, and then, the changes in the impedance responses were evaluated over exposure time. EIS was carried out in the 100 kHz to 100 mHz frequency range (36 points) using 10 mV peak-to-peak voltage amplitude for 16 weeks of immersion to evaluate the long-term corrosion behavior and the data were fitted and analyzed by the Zview software (version 3.1).

Tribocorrosion properties

The tribocorrosion properties of the substrate and oxidized specimens were determined on the tribo-electrochemical machine using a SiC ball (Ø = 5 mm) at a normal load of 10 N, speed of 0.1 m/s for 40 m, 5 mm stroke length, and 1 Hz oscillating frequency. Each test was repeated 3 times. The EG&G potentiostat/galvanostat model 263A was utilized to measure OCP as a function of immersion time. The PBS solution (pH = 7.4 ± 0.1) was used in the tribocorrosion tests at 37 °C. Immersion for 24 h was required to reach the steady-state OCP and the OCP was then recorded for 10 min before sliding, 20 min during sliding, and 10 min after sliding.

Results and discussion

Characterization of the oxidized specimens

Figure 2 presents the XRD patterns of the Zr–2.5Nb alloy after oxidation under different conditions. As shown in Fig. 2, after processing for 3 h at 523 °C, a ZrO_2 layer was formed on the surface of the Zr–2.5Nb substrate. Several papers [23–25] have discussed the phase composition of the PEO coatings formed on pure zirconium and zirconium alloys. According to XRD results, the oxide layer mostly consists of monoclinic zirconia (*m*-ZrO_2, JCPDS card no 37–1484) with a small amount of tetragonal phase (*t*-ZrO_2,

Table 2 Chemical composition, thickness, the surface roughness of the oxide coatings, and crystallite size of $(\bar{1}11)_m$ and $(101)_t$ planes extracted from XRD patterns

Specimens	Elements (at.%)			Oxide layer thickness (μm)	Roughness (R_a) (μm)	FWHM (°)		Crystallite size (nm)	
	Zr	Nb	O			$(\bar{1}\,11)_m$	$(101)_t$	$(\bar{1}\,11)_m$	$(101)_t$
OX1	33.63	2.79	63.54	3.03 ± 0.1	0.19 ± 0.08	0.561	0.812	89.4 ± 11	43.6 ± 12
OX2	34.16	2.27	63.57	5.09 ± 0.2	0.21 ± 0.09	0.515	0.780	90.6 ± 9	49.4 ± 11
OX3	34.03	2.46	63.60	5.96 ± 0.2	0.26 ± 0.09	0.438	0.682	98.3 ± 9	54.8 ± 8
OX4	33.10	2.79	64.11	20.02 ± 0.2	0.75 ± 0.11	0.411	0.625	178.6 ± 14	83.2 ± 11
OX5	33.18	2.46	64.36	85.82 ± 0.7	1.21 ± 0.16	0.210	0.481	382.9 ± 33	101.4 ± 23

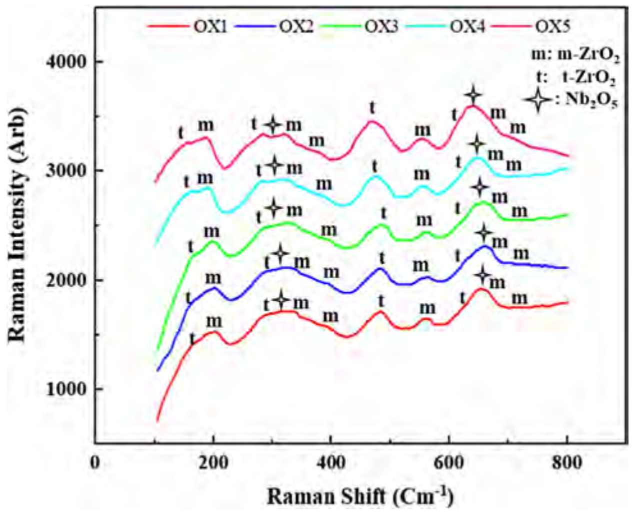

Figure 3 Raman scattering spectra of the oxide coatings.

JCPDS card no 42–1164). Furthermore, in all oxide layers, Nb_2O_5 was detected. The intensity of the *t*-ZrO_2 peaks decreased as the oxidation temperature increased due to the volume expansion that occurred during the monoclinic to tetragonal phase change which restricted further transformation as the available space decreased [25]. Hobbs et al. [23] reported that in addition to the major oxide phase of monoclinic *m*-ZrO2, a small amount of tetragonal *t*-ZrO2 has formed, as evidenced by the (111)*t* peak. Also, the 6 h 635 °C oxide showed possible evidence of Nb2O5 formation in the two small peaks either side of 2θ = 29°. Table 2 represents the chemical composition of the oxide coatings. The concentration of Zr and O elements is between 33.10 to 34.16 and 63.53 to 64.36 at.%, respectively, and the concentration of Nb element in the oxide coatings remains at 2.3–2.8 at.% as the temperature is increased from 523 to 800 °C. The O/Zr atomic ratio is approximately 1.7–2, indicating the presence of the ZrO_2 phase [25]. Similar results have been reported before showing the major m-ZrO_2 phase with trace amounts of *t*-ZrO_2 [24].

To confirm the XRD and EDS results and delicately specify the phases present in the oxide layers of each specimen, Raman spectra are compared as shown in Fig. 3. The bands at 148, 266, 474, and 637 cm^{-1} correspond to those of tetragonal zirconia [26, 27], whereas those at 181, 330, 380, 475, 558, 615, 690, and 760 cm^{-1} are related to monoclinic ZrO_2 [28, 29]. However, Raman Spectroscopic assessment shows the detection of the only tetragonal phase in the wear zone of ZrO2/7-Mrad after 10Mc [15]. The bands at 280 and 650 cm^{-1} indicate the presence of Nb_2O_5 in the coating (Fig. 3) confirming the XRD results [28]. Cao et al. [30] have reported that Raman spectra of Nb_2O_5 are similarly dominated by a broad band at around 700 cm^{-1}. Figure 3 shows that 800 °C is not high enough to convert the tetragonal phase to the monoclinic phase, so both phases are observed by increasing the annealing temperature. In order to determine the simultaneous existence of Zr–O–Zr and Nb–O–Nb bonds in the oxidized layers and the difference between the coatings formed at different temperatures, the regions of 100–450 and 450–800 cm^{-1} are deconvoluted in OX1, OX4, and OX5 specimens (Fig. 4) [31]. As the oxidizing temperature increases from 523 to 800 °C, the intensity of *t*-ZrO_2 and Nb_2O_5 bonds increases which represents the higher amounts of these phases in the oxidized layer, especially in the OX5 specimen.

The surface morphology and cross section of the oxide coatings are displayed in Figs. 5a–e′. At 523 °C, the black coatings displayed a similar structure for different oxidation times. At higher temperatures, the microscale grooves and uniformly oriented scratches appear in the surface morphology as observed in OX4 and OX5 specimens. According to Fig. 5e′, multiple cracks and upheaved areas formed in the OX5 specimen, and the macroscopic color of the coating

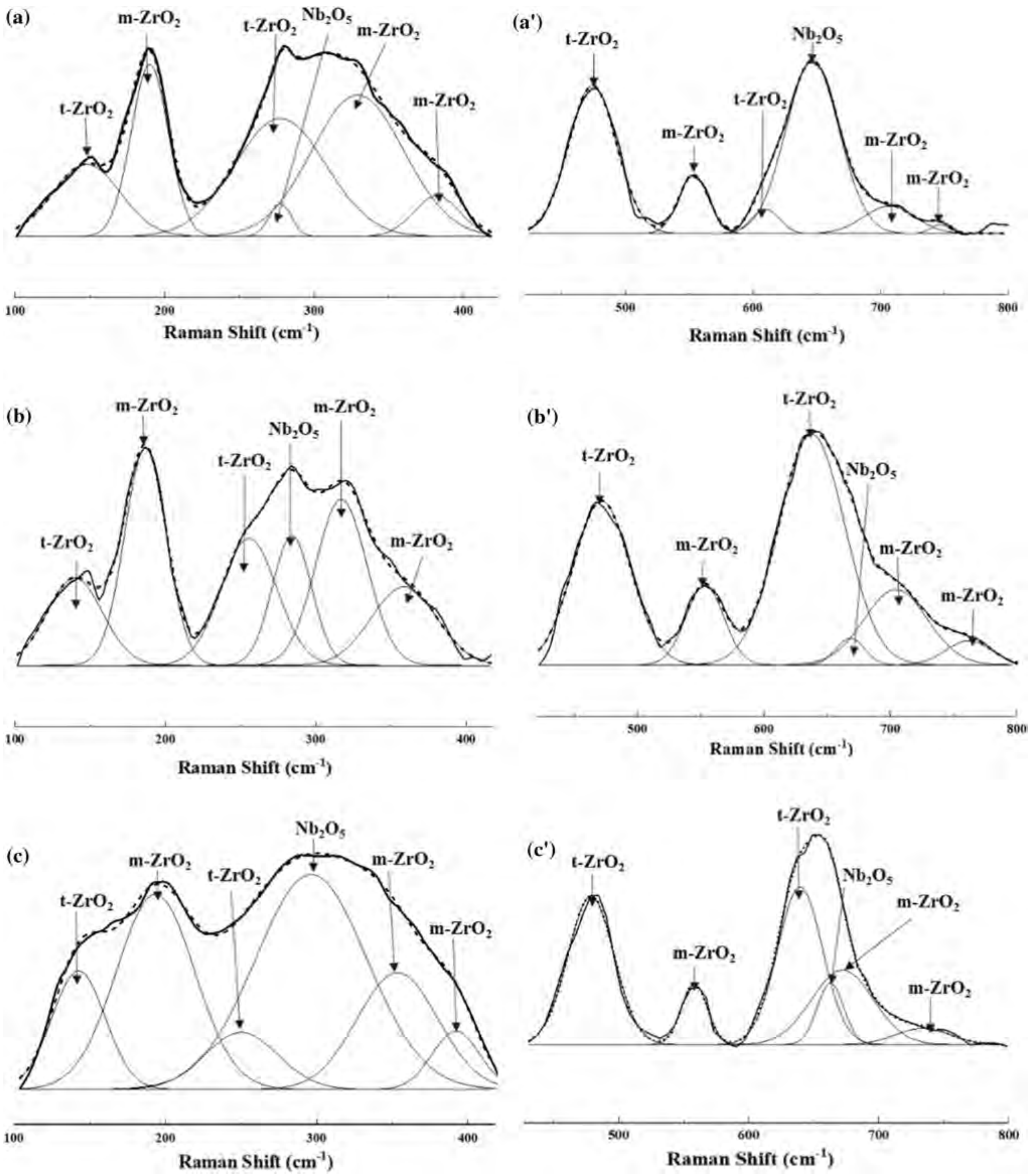

Figure 4 Deconvoluted Raman spectra of **a**, **a′** OX1, **b**, **b′** OX4, and **c**, **c′** OX5 in the range of 100–450 and 450–800 cm.$^{-1}$.

changed to light gray (approximately white) while the coating was starting to delaminate from the substrate due to the high operating temperature. The metallic surface transforms into a dense ceramic that is predominantly m-ZrO_2 during oxidation [32] according to $Zr + O_2 \rightarrow ZrO_2$ (ΔH = –1100 kJ/mol at 298 K), which is a diffusion-controlled process. The proposed mechanism for diffusion includes O_2 adsorption/desorption at the metal/air interface, diffusion/dissolution of O_2, formation of an oxide

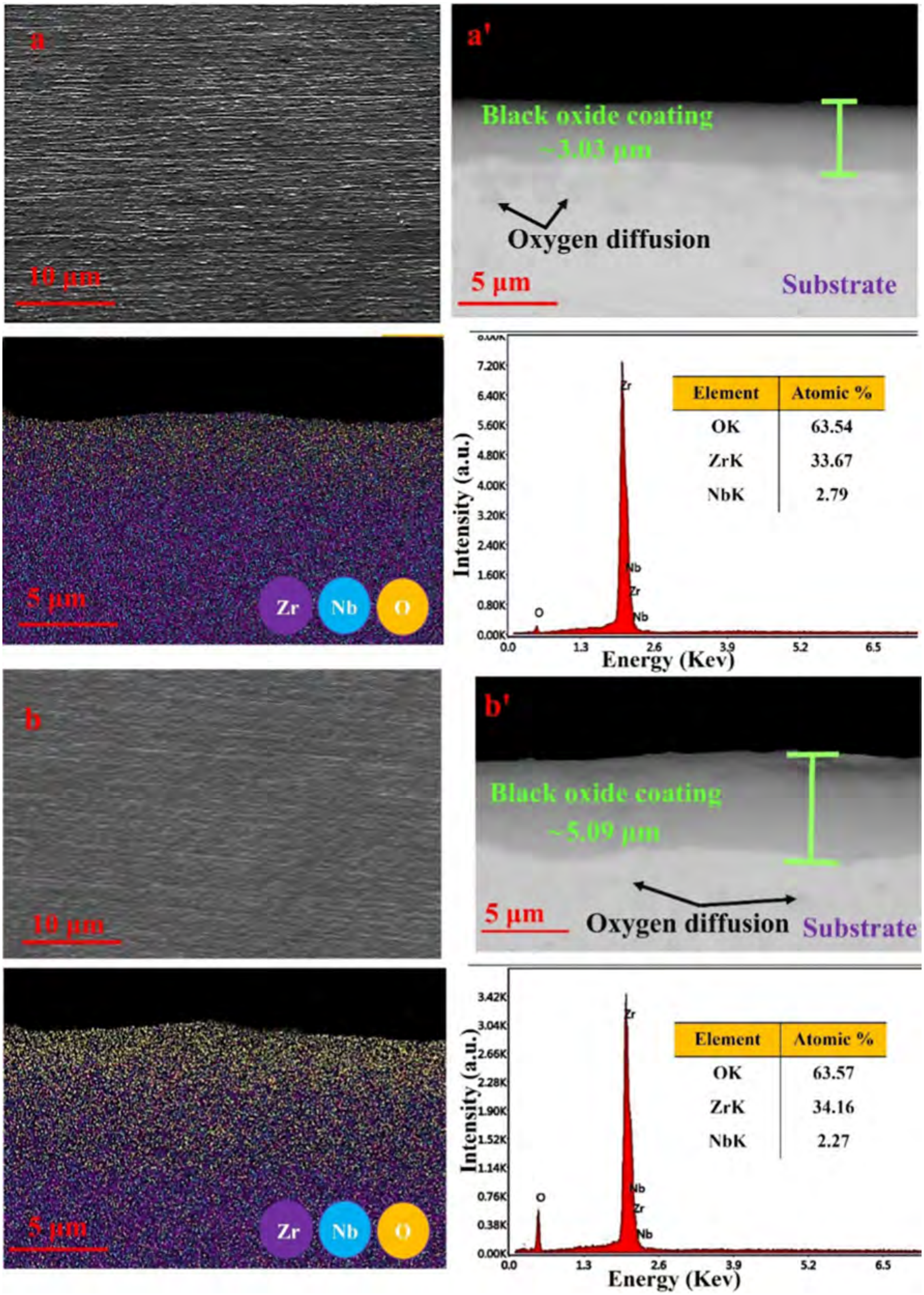

Element	Atomic %
OK	63.54
ZrK	33.67
NbK	2.79

Element	Atomic %
OK	63.57
ZrK	34.16
NbK	2.27

Figure 5 Surface morphology **a**–**e** and cross-sectional images including EDS spectra (from the coating region), and elemental mapping **a′**–**e′** of the specimens: **a**, **a′** OX1, **b**, **b′** OX2, **c**, **c′** OX3, **d**, **d′** OX4, and **e**, **e′** OX5.

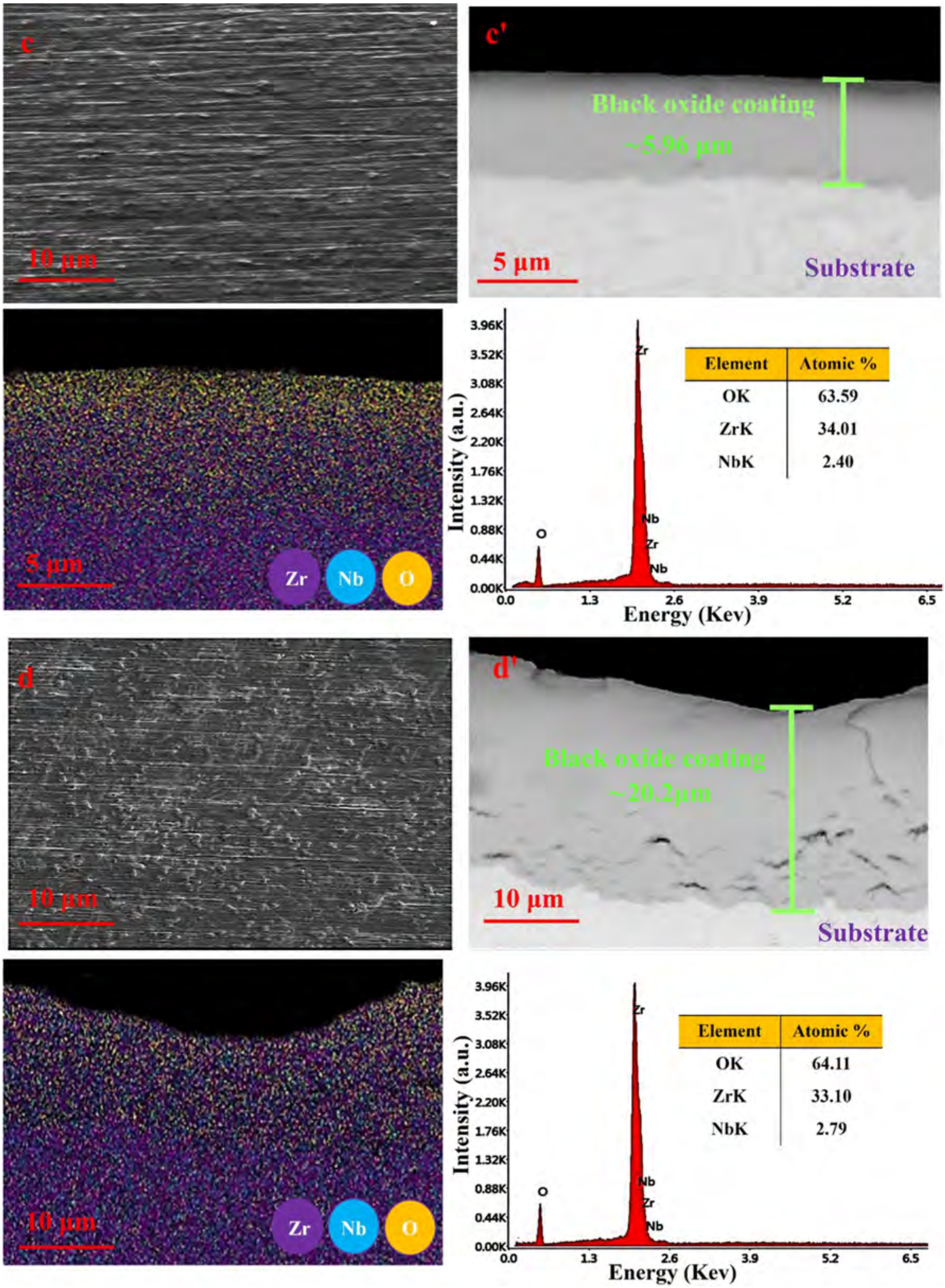

Element	Atomic %
OK	63.59
ZrK	34.01
NbK	2.40

Element	Atomic %
OK	64.11
ZrK	33.10
NbK	2.79

Figure 5 continued.

layer, oxygen diffusion through the oxide layer, and oxide growth on the metal/oxide interface as described in Fig. 6.

As shown in Fig. 5, the thickness of the oxide layer and surface roughness increase with oxidation temperature. The oxide layers grown at lower

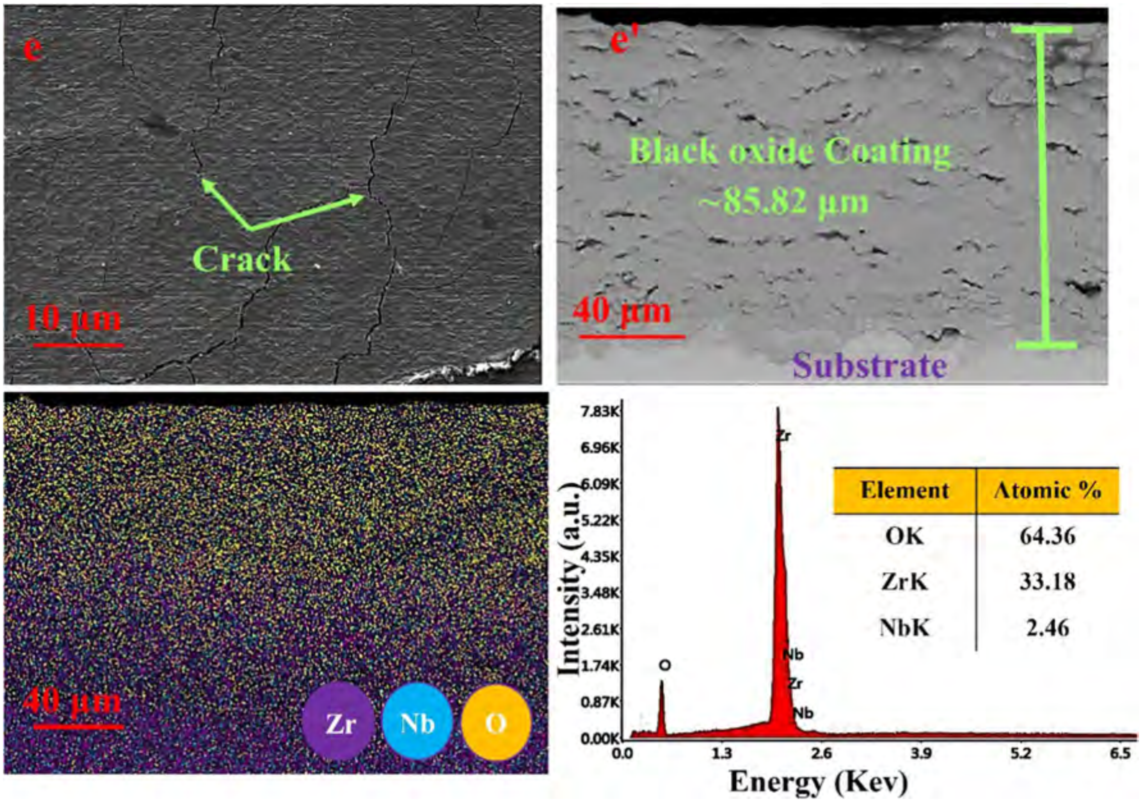

Figure 5 continued.

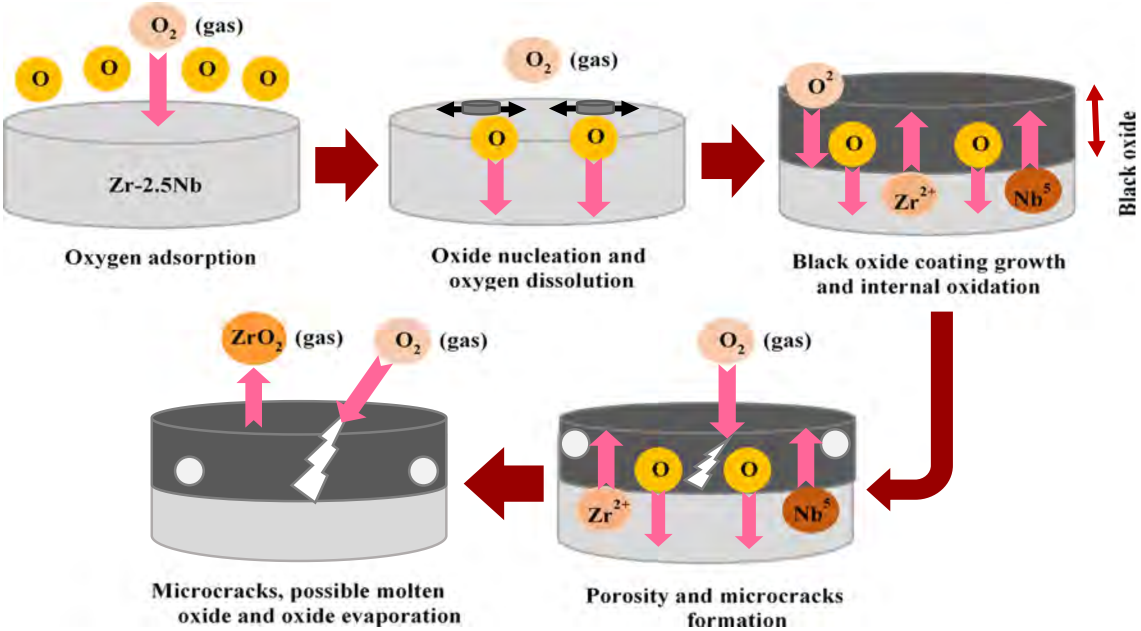

Figure 6 Schematic representation of ZrO2 oxide layer formation.

temperatures (Figs. 5a–c') are thin, continuous, and more compact. However, the surface of the oxide coatings shows microcracks due to the smaller coefficient of thermal expansion of ZrO_2 compared to the substrate. This means the temperature change introduces thermal stress in the oxide layer. In combination with the growth stress caused by coarsening of plate-like oxides, cracks are formed in the oxide layer

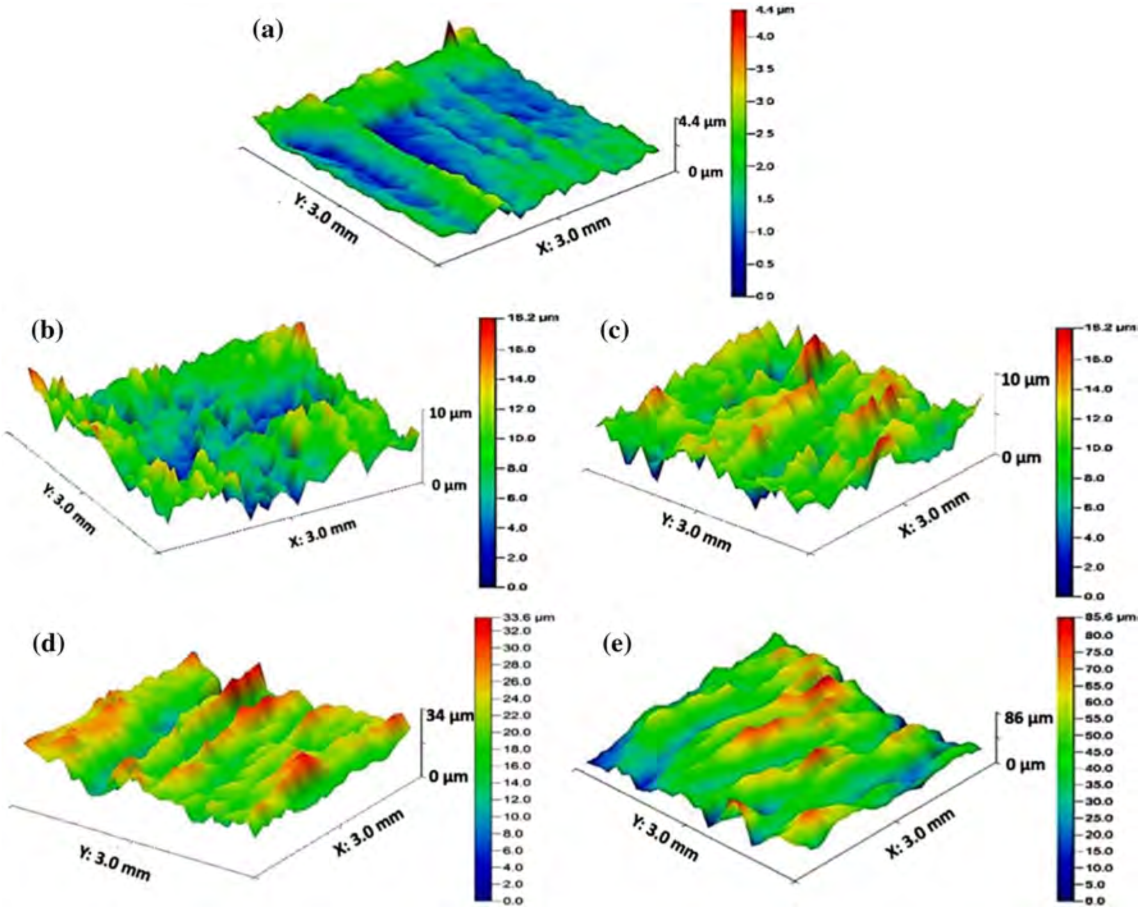

Figure 7 3D profiles of the surface topography of oxide coatings in different conditions: **a**: OX1, **b**: OX2, **c**: OX3, **d**: OX4, and **e**: OX5.

[33]. The higher oxidation rate may stem from oxidant diffusion along the cracks in the oxide layer to promote the oxidation [34].

The crystallite size of the monoclinic and tetragonal phases are calculated from $(\bar{1}\,11)_m$ and $(101)_t$ planets located at 2θ angles of 28.2 and 30.2°, respectively (Table 2). As seen, increasing the temperature and time of oxidation causes crystallite growth. The results demonstrate that the crystallite size growth is more significant by raising the temperature to 800 °C in the OX5 specimen (to 382.9 ± 33 and 101.4 ± 23 nm for $(\bar{1}\,11)_m$ and $(101)_t$ peaks for the OX5 specimen, respectively). The relative densities of the OX1, OX2, OX3, OX4, and OX5 specimens are about 99.2, 99.5, 99.7, 92.9, and 86.5% (± 0.1), respectively. Due to the presence of several cracks in the oxidized specimens (especially in the OX5 specimen), determining exact values was difficult, therefore, the tests were repeated several times.

Figure 7 displays the 3D surface topography of the oxide coatings formed under different conditions.

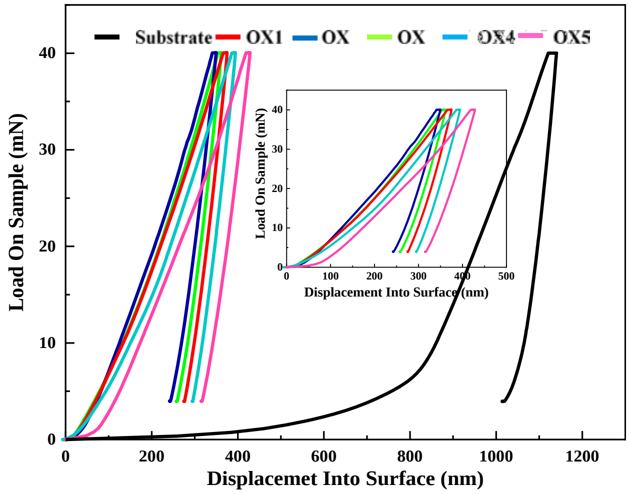

Figure 8 Load-indentation depth curve and comparison between the substrate and oxide coatings.

The surface roughness affects the suitability of knee implants after implantation [35]. Although the surface roughness increases considerably by increasing

Table 3 Nanohardness (H), Young's modulus (E), Knoop microhardness, and H/E ratio of the specimens

Specimen	Elastic Modulus (GPa)	Nanohardness (GPa)	Knoop microhardness (HK_{25})	H/E ratio
OX1	218.67 ± 18.06	11.14 ± 1.01	1078.7 ± 93.0	0.055
OX2	249.03 ± 23.81	19.92 ± 4.15	1381.3 ± 185.4	0.080
OX3	238.64 ± 21.88	17.89 ± 3.06	1328.3 ± 197.5	0.074
OX4	225.95 ± 19.01	13.45 ± 2.11	1206.3 ± 105.3	0.070
OX5	200.27 ± 15.06	11.01 ± 1.20	1012.4 ± 106.6	0.054

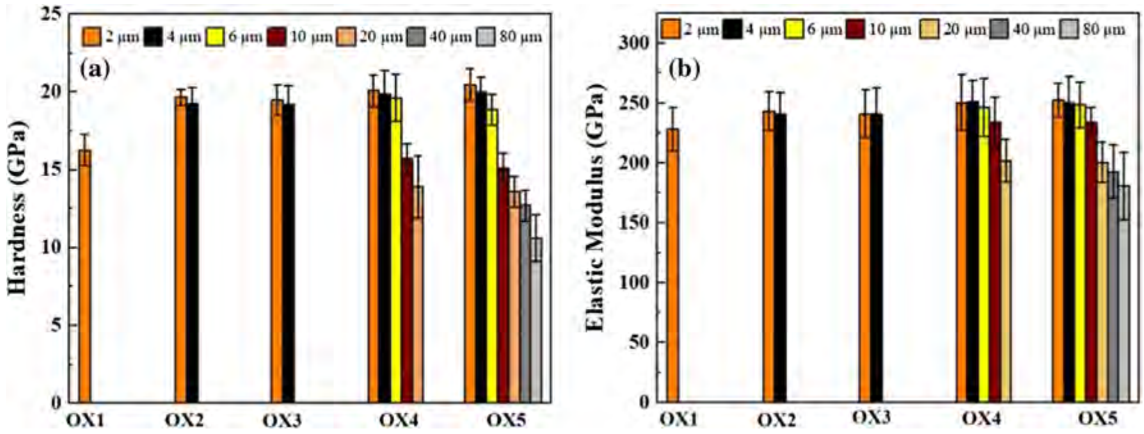

Figure 9 **a** Hardness and **b** elastic modulus value of the coatings at different depths or distances of the indents from the metal-coating interface.

the oxidation time at 523 °C, it is still considered suitable for osseointegration and hence, surface roughness between 100 and 1000 nm and thickness between 5 and 20 μm are acceptable [14, 36]. Nakonieczny et al. [35] reported the lowest surface roughness was characterized by reference.

samples (Ra = 32 nm), while the higher roughness was found in the sample after the accelerated.

aging process, t = 2.5 h (Ra = 61 nm).

Mechanical properties of ZrO_2 coatings

The hardness of the bare and coated Zr–2.5Nb alloy is measured on both the microscale and nanoscale. The loading–unloading characteristics of the substrate and oxide layers are determined by the nanoindentation technique at a maximum load of 40 mN. By withdrawing the indenter from the surface in 20 s, the penetration depth is less than 10% of the oxide layer thickness [35]. The nanoindentation and Knoop microhardness results are summarized in Fig. 8 and Table 2. The coating hardness and Young's modulus are influenced by coating characteristics such as thickness, composition, pores, and microcracks [37]. The highest nano and microhardness are observed from OX2 (treated at 523 °C for 4 h), which are close to those of OX3 (treated at 523 °C for 5 h) due to the low surface roughness and uniform thickness. The hard t-ZrO_2 phase is responsible for the intrinsic hardness of OX2 (19.92 ± 4.15 GPa).

Similar hardness values of ~ 1100 HV have been reported by Chen et al. [32, 33] using the air plasma spraying and plasma electrolytic oxidation technique [34, 38]. Yong's modulus for oxidized specimens between 200 and 250 GPa, that is corresponding to the provided data.

[34] indicates in this study, the extreme values of these properties are taken.The nanohardness test indicates that the OxZr hardness is more than twice that of CoCr on the articulating surface. However, it is noted that this alone does not imply a higher abrasion resistance [32, 39]. The surface pores and microcracks result in lower hardness for OX5 (Table 2).

The hardness-to-elastic modulus ratio is known as the plasticity index and is one of the important

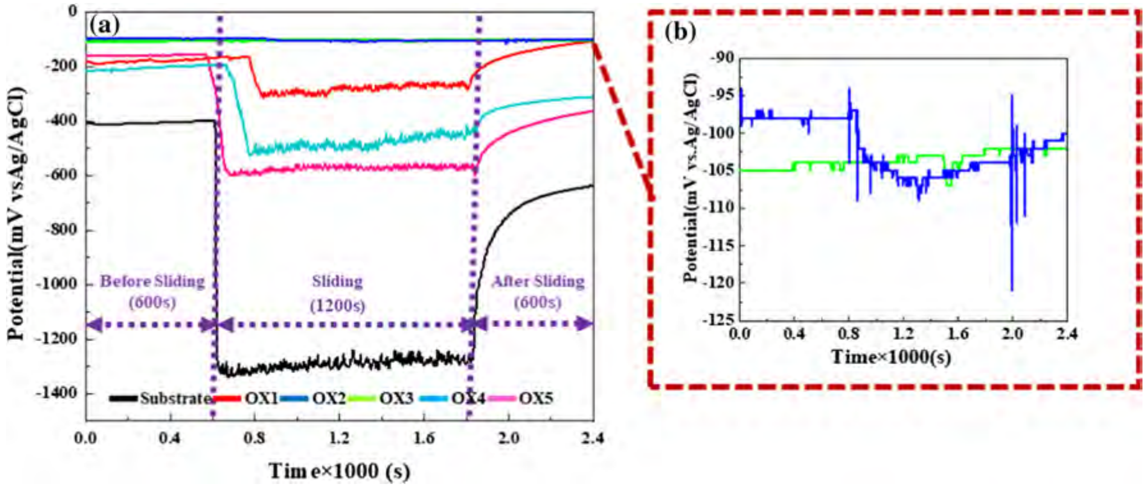

Figure 10 Variations of OCP before, during, and after sliding in the PBS solution, **a** for all the specimens and **b** OX2 and OX3 specimens.

parameters affecting the elastic behavior of the contact surface. A larger H/E ratio implies better wear resistance [40]. Table 3 shows the H/E ratios of different specimens derived from results obtained by the nanoindentation tests. OX2 (0.080) shows the biggest H/E ratio and OX5 have the smallest value.

Figure 9 presents the nanoindentation results for different thicknesses. The nanohardness of the zirconia layer ranges from 14 to 20 GPa, which is much higher than the Zr-2.5Nb bare substrate is about 4–7 GPa [41] along the area of oxygen diffusion. In the inner layer close to the interface (2 μm from the interface), an increase is observed at higher oxidation temperature related to the higher degree of densification. As the distance from the interface is increased to 6 μm, the hardness and elastic modulus change slightly due to the low porosity gradient and uniform oxide layer. Moreover, concerning the ZrO_2 film formed on the zirconium alloy, part of the tetragonal phase transforms into the monoclinic phase thus producing high internal stresses around the transformed ZrO_2 crystallites due to the transformation strain [42].

The porosity gradient has a detrimental effect on Young's modulus and hardness [43]. In the OX1, OX2, and OX3 specimens with less than 6 μm thicknesses, the relative density is up to 99%. After 60 min at 523 °C, the hardness (19.68 ± 0.5 GPa) of the OX3 specimen drops slightly to 19.49 ± 1 GPa because the decrease in the volume fraction of t-ZrO_2 is more slowly with increasing time [24, 44]. On the other hand, as for the OX4 and OX5 specimens, with increasing distances from the interface, the crystallite size increases, and a gradual reduction in the hardness and elastic modulus are observed. The coating hardness is influenced by the microstructure of the coatings including pores and microcracks [37]. For the OX4 specimen with increasing the coating thickness of 2, 4, 6, 10, and 20 μm from the interface, the hardness value reached 20.1 ± 2, 19.89 ± 1, 19.64 ± 2, 15.7 ± 1, 13.6 ± 3, and 13.9 ± 2, respectively, regarding this trend was observed for elastic modulus 250 ± 23, 251 ± 18, 246.7 ± 24, 234.3 ± 21, 202 ± 18. OX5 specimen followed a similar trend of hardness and elastic modulus profiles, where decreases of both measured properties are detected at distances up to 4 μm of the interface. The coating layer at a distance of 80 μm had the lowest value of hardness and elastic modulus 10.6 ± 1, and 180.8 ± 28 GPa, respectively. Consequently, large pores and microcracks near the surface result in lower hardness for the OX4 and OX5 specimens, whereas the dense layer close to the interface/coating exhibits higher hardness and elastic modulus.

Tribological investigation

The tribocorrosion test is performed at OCP in the PBS solution adjusted to a pH of 7.4 ± 0.1. Figure 10 shows the change in the potential with time under open-circuit conditions after immersion for 24 h in PBS at 37 °C. There are three different stages before, during, and after sliding. When SiC ball sliding commences, the OCP shows no appreciable changes for OX2 and OX3. At the end of sliding, the OCP remains unchanged implying a lack of exposure of

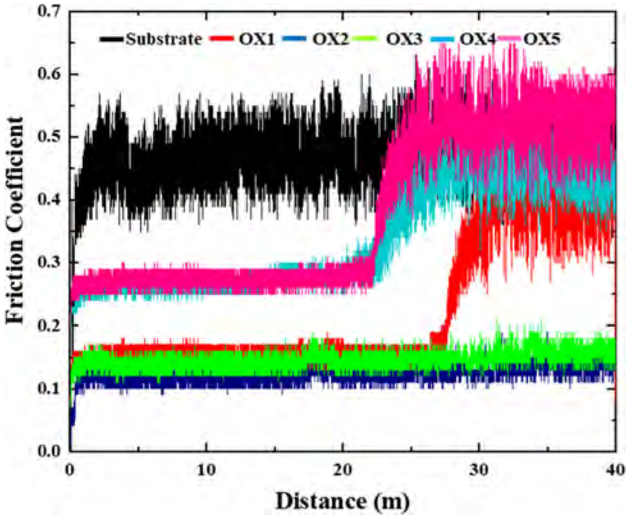

Figure 11 Friction coefficients of the substrate and oxide coatings against the SiC ball.

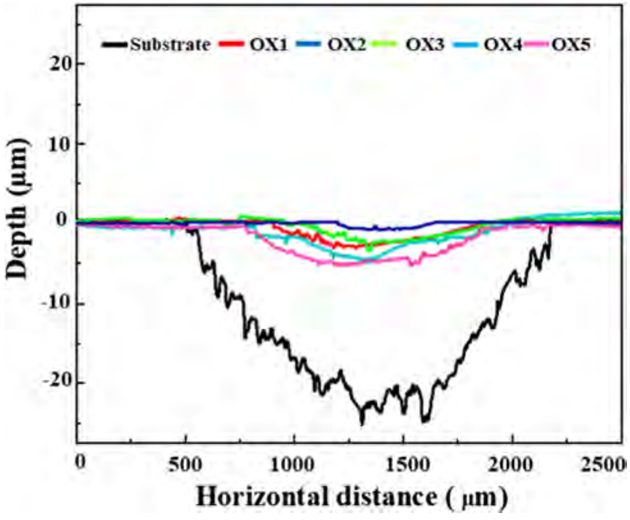

Figure 12 Line profiles of the wear scars after the tribocorrosion tests.

new materials to the electrolyte despite the ball sliding on the surface. The potential fluctuations during sliding can be caused by the ball movement in PBS or instant partial delamination of the tribolayers [44]. However, the substrate OCP decreases to more negative values at the onset of sliding before increasing gradually until the end of sliding (1200 s). It can be the result of scratching at the onset of sliding that removes the passive film and exposes the active surface of the Zr–2.5Nb substrate to the electrolyte followed by repassivation. Here, the strong OCP fluctuation during sliding can be explained by the dynamic equilibrium between depassivation and repassivation on the worn surface [45]. As for OX4 and OX5, a slow decrease of OCP is observed during sliding. The OCP drop at the onset of sliding is due to the mechanical destruction of the coating layer upon initial impact with the ball creating local exposure to the aggressive solution on the bare Zr–2.5Nb alloy substrate. This in turn creates galvanic couples among the corroded and un-corroded surfaces in the wear scar [46]. The bare area developed by further sliding increases the anode area in the wear scar resulting in a further decrease in the OCP. These results indicate that the oxide layers offer better tribocorrosion resistance.

Figure 11 presents the changes in the coating's friction coefficients (COF) versus displacements during the tribocorrosion test under a 10N normal load. The OX5 specimen shows the highest COF due to the highest porosity percentage (~13.5%) and Ra (~1.21 μm) thus reducing the contact between SiC and the coating surface. The COF change includes several stages such as plowing wear, abrasive wear, and adhesive wear [47]. The first stage is the contact of the SiC counter body with the outer porous layer in the OX4 and OX5 specimens with large thicknesses together with pores and surface roughness. After polishing and removing the outer layer, the ball contacts the inner layer with higher compactness, hardness, and less roughness. Owing to the small thickness of the inner layer (5–10 μm) and the formation of wear debris, COF continues to increase and reaches a maximum value. Then the coating is broken and damaged, where the substrate is completely evident at a ~20 m distance. The substrate is worn until 40 m and the COF of the substrate is recorded. OX4, OX5, and the substrate exhibit obvious fluctuations due to the higher surface roughness which produces higher wear debris. However, the OX2 and OX3 specimens show slightly worn, smaller friction coefficients with no significant fluctuations due to the higher hardness, larger H/E ratio, and perhaps smaller roughness. In the OX1 specimen, by increasing the contact of the counter body with the coating layer, the coating is slightly damaged and broken at some points leading to increase COF, and ultimately the coating is completely broken after the ~28 m distance. In the OX2 and OX3 specimens, the coating remains stable for the whole sliding distance showing higher wear resistance than other coatings [48].

Figures 12 and 13 depict the linear average profiles and SEM images across the wear tracks after the tribocorrosion tests that were examined using a

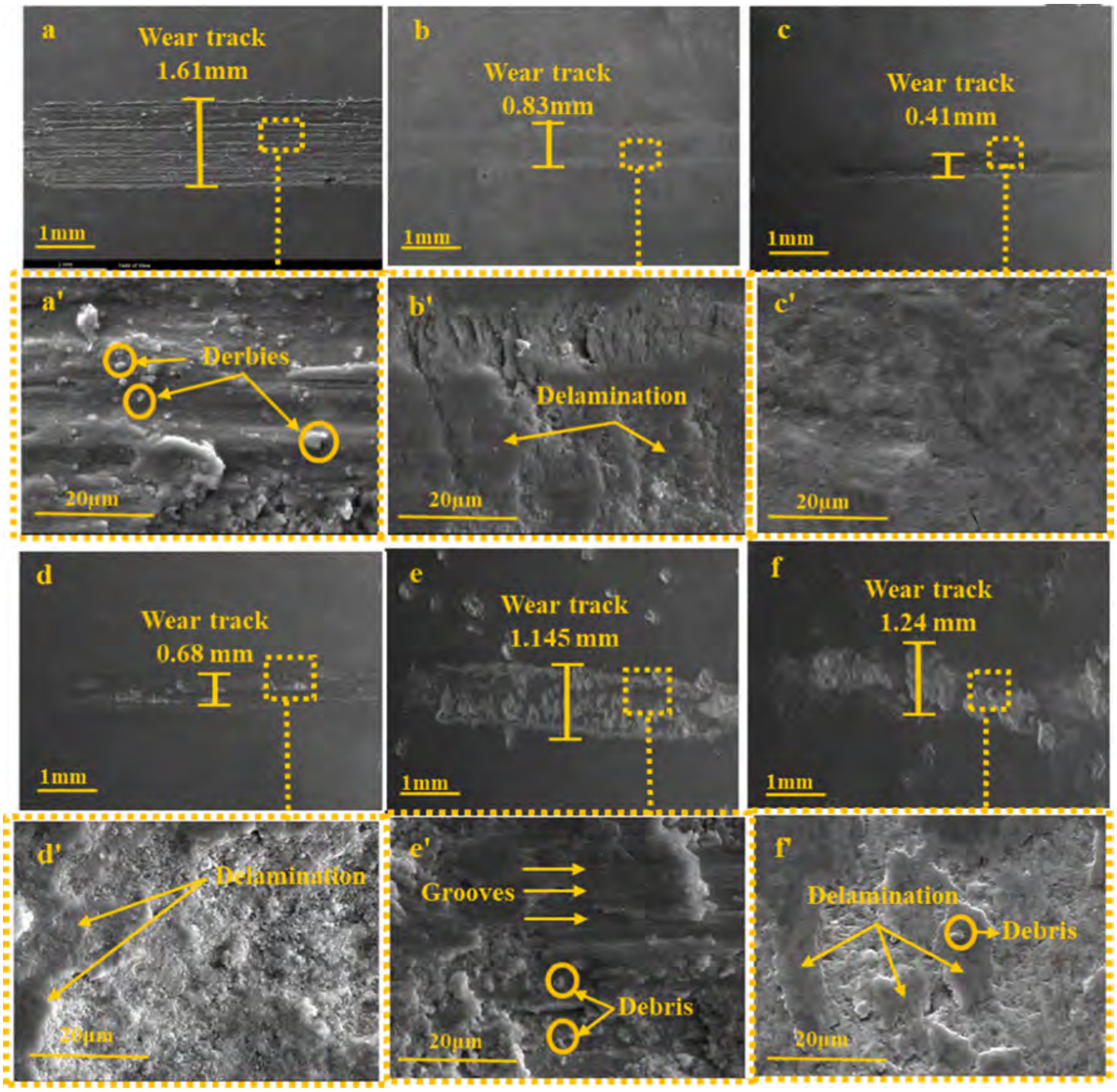

Figure 13 SEM images of the wear scars: **a**–**a**′ substrate, **b**–**b**′ OX1, **c**–**c**′ OX2, **d**–**d′** OX3, **e**–**e′** OX4, and **f**–**f′** OX5 after the tribocorrosion tests at OCP.

profilometer. The line profiles across the wear tracks are used to calculate the volume loss. The volume losses of OX1, OX2, OX3, OX4, and OX5 are 0.0725, 0.046, 0.061, 0.095, and 0.11 mm^3, respectively, indicating that OX2 has the smallest volume loss. This confirms the improvement in the tribocorrosion resistance for larger *t*-ZrO$_2$ harder phase incorporation. As shown in Fig. 12, the Zr–2.5Nb bare specimen shows the highest track width and depth (~25.0 µm) even larger than the coating thickness (~80 µm), where many grooves and parallel scratches are visible (Figs. 12a-a′). This indicates that the wear process completely removes the coating. Thereafter, the substrate is worn and the adhesive wear mechanism prevails as confirmed by increased fluctuations in the friction coefficients [49].

The hardness of the coating might affect the wear resistance, which is controlled by the phase composition and porosity levels [50]. In the OX4 and OX5 specimens, lower hardness, higher R_a, and porosity percentage result in high debris (tribo-products) during the wear test (see Figs. 13e′ and f′) that causes the three-body wear phenomenon leading to fast removal of the coating [33]. To investigate the wear mechanism of the ceramic coatings, the wear tracks generated on the coated worn surfaces are examined by SEM as shown in Fig. 13. Based on the images of the worn tracks (Fig. 13), the debris can be ejected

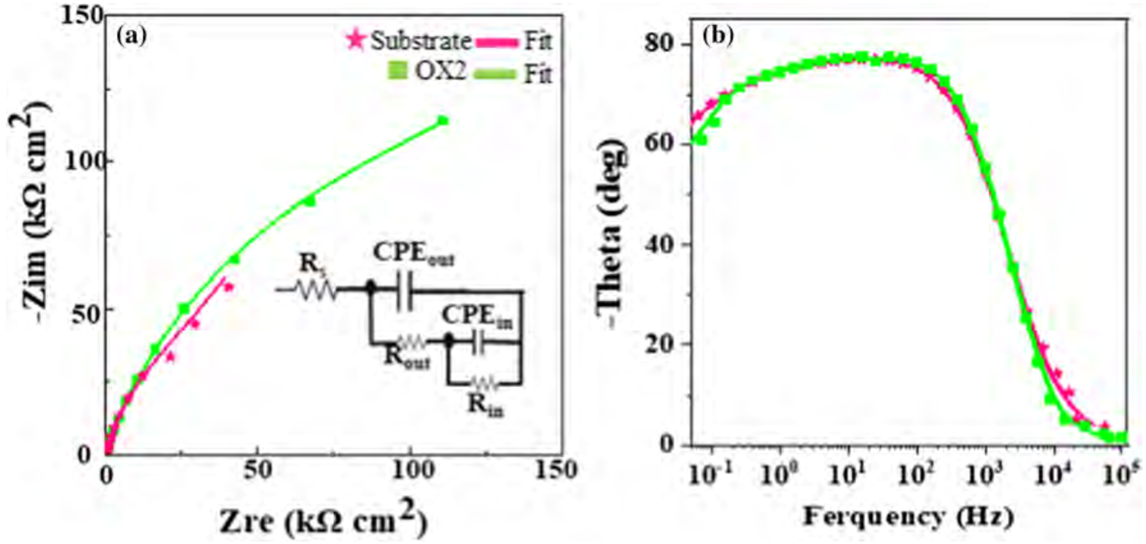

Figure 14 **a** Nyquist and **b** bode-phase plots of OX2 in PBS solution at pH 7.4 after immersion for 24 h.

from the friction area easily. The abrasive particles and removed materials indicate abrasive and adhesive wear for the substrate, OX1, OX4, and OX5. During sliding, the debris generated on OX1, OX4, and OX5 fill the larger flaws and the rest of the spalling particles are engaged in the wear process. In fact, plastic deformation proceeds in the wear test due to the formation of cracks on the surface. Crack propagation results in the separation of particles from the surface. Furthermore, there are uneven surfaces and many parallel scratch grooves related to continuous and repeated delamination of the coating and debris.

The worn regions on the substrate, OX1, OX4, and OX5 show severe abrasion and plastic deformation caused by the scratching action of the SiC ball. On the other hand, the worn surfaces on OX2 and OX3 manifest as smooth and dull areas, indicating that these coatings with high density and low roughness, show a higher wear resistance. The small depth of track (<2 μm) indicates that a considerable part of the coatings is undamaged until 40 m.

Corrosion resistance

EIS tests were carried out in PBS solution (pH 7.4 ± 0.1) on the OX2 specimen as the optimal one due to its best mechanical and tribological properties among other specimens. Furthermore, previous researches [38, 51] indicate the oxidation rate of the zirconium oxidized in air atmosphere is increasing with the increase in the temperature and exposure time. Initially, oxidation follows a parabolic rate at all temperatures above 700 °C. EIS is a non-destructive technique for probing the electrode–electrolyte interface and provides the means of determining the contributions of the oxide film, resistance, and capacitance to the total impedance of the system [52]. The short-term impedance test results after immersion for 24 h are presented in Fig. 14. The Nyquist diagrams of the Zr–2.5Nb substrate and oxidized specimens exhibit incomplete semi-circles denoting full barrier characteristics. The corresponding Bode-phase diagrams (Fig. 14b) at high angles (~ 80°) show wide regions with two distinguished overlapping humps that are raised by the passive oxide layer which consists of an outer porous layer and an inner compact layer.

The EIS spectra were analyzed based on the electrical equivalent circuits. The proposed electrical equivalent circuit inserted in Fig. 14a involves two parallel time constants and Rs which represent the resistance of the PBS solution [53]. Owing to the surface heterogeneity, CPE is used instead of the ideal capacitor (C) in the equivalent electrical circuit to compensate for the non-homogeneity in the system. R_{in} determines the charge transfer resistance and CPE$_{\text{in}}$ determines the electrical double layer capacity at the oxide layer/substrate interface. The extracted data from EIS plots are represented in Table 4. According to Table 4, the R_{in} and R_{out}, representing the oxide layer barrier resistance at lower and higher frequencies, respectively, increase by forming the

Table 4 EIS data of the substrate after immersion for 24 h and OX2 after immersion for different times of 24 h, 1, 4, 8, 12, and 16 weeks in the PBS solution (pH = 7.4 ± 0.1)

Specimens	Immersion time	Outer layers			Barrier layers				
		CPE_{out} ($\mu F.cm^{-2}.S^{n-1}$)	n_{out}	R_{out} ($k\Omega.cm^2$)	CPE_{in} ($\mu F.cm^{-2}.S^{n-1}$)	n_{in}	R_{in} ($M\Omega.cm^2$)	R_{Total} ($M\Omega.cm^2$)	χ^2
Bare		0.78 ± 0.01	0.71 ± 0.03	10.28 ± 0.21	0.30 ± 0.01	0.68 ± 0.03	0.30 ± 0.31	0.310 ± 0.021	2.1E-4
OX2	24 h	1.82 ± 0.02	0.78 ± 0.01	12.26 ± 0.17	0.41 ± 0.03	0.71 ± 0.07	0.36 ± 0.01	0.372 ± 0.034	0.1E-3
	1-week	5.37 ± 0.01	0.91 ± 0.02	43.09 ± 0.73	1.33 ± 0.02	0.95 ± 0.05	6.31 ± 0.07	6.353 ± 0.102	0.3E-4
	4-week	2.61 ± 0.03	0.89 ± 0.09	40.68 ± 0.19	1.29 ± 0.26	0.91 ± 0.07	5.04 ± 0.13	5.080 ± 0.192	0.6E-4
	8-week	2.72 ± 0.03	0.86 ± 0.03	36.04 ± 0.07	1.28 ± 0.03	0.89 ± 0.03	5.01 ± 0.05	5.046 ± 0.10	1.3E-3
	12-week	1.47 ± 0.04	0.85 ± 0.06	28.51 ± 0.11	2.69 ± 0.12	0.89 ± 0.01	4.33 ± 0.82	4.332 ± 0.021	0.3E-4
	16-week	4.10 ± 0.03	0.82 ± 0.02	26.38 ± 0.02	1.61 ± 0.03	0.86 ± 0.03	4.16 ± 0.19	4.186 ± 0.175	1.0E-4

oxide layer on the surface of the substrate (compare Zr–2.5Nb substrate and OX2-24 h specimens). The grain in the ZrO_2 film formed on zirconium alloys mainly has two morphologies: columnar in the internal layer near the oxide/metal interface and equiaxed in the cracked outer layer [41]. R_{out} which illustrates the outer porous layer of the ZrO_2 coating is only 360 kΩ $cm^{2,}$ whereas R_{in} is 98 MΩ cm^2 which indicates the excellent barrier performance of the inner layer.

The EIS spectra are recorded for longer immersion times of 4, 8, 12, and 16 weeks to investigate the electrochemical properties of the ZrO_2 coatings and their stability in the biological environment. The Nyquist plots during 16 weeks of immersion in PBS solution are represented in Fig. 15a. According to Fig. 15, the bode-phase diagrams of all specimens consist of two humps at low and high frequencies, representing the inner and outer layer time constants, respectively. The hump present at lower frequencies consists of two humps that merged and formed one hump and are formed due to the inner compact layer of the oxidized coating and electrical double-layer response. The one at higher frequencies is attributed to the outer porous layer of the oxidized coating. As shown in Fig. 15b, a maximum is observed at high frequencies after 1 week of immersion in PBS solution at 37 °C. After 1 week of immersion in PBS solution, the corrosion products plug the cracks present on the surface of the oxide coatings, and the corrosion resistance value increases. However, by increasing the immersion time, the corrosion resistance decreases again due to the penetration of aggressive ions through the coating imperfections. By continuing the time to 8 weeks, as shown by the Bode-phase curves, the phase angles decrease at frequencies less than 1 Hz, representing the decay in the barrier performance of the barrier layer.

The results confirm that R_{in} at a longer time has the order of $M\Omega.cm^2$ and plays an effective role in corrosion resistance. Therefore, both the inner and outer layers affect the barrier performance of the coatings. Hence, the total coating resistance, $R_T = (R_{in} + R_{out})$, can be used to describe the barrier effect of the coatings. The chi-square (χ^2) values shown in Table 4 reveal the magnitudes < 0.003 indicating the best fitting of data. According to Table 4, the R_T of the coating is quite large and increases with exposure time after 16 weeks indicative of gradual loss of the barrier performance of the coating. However, R_T after

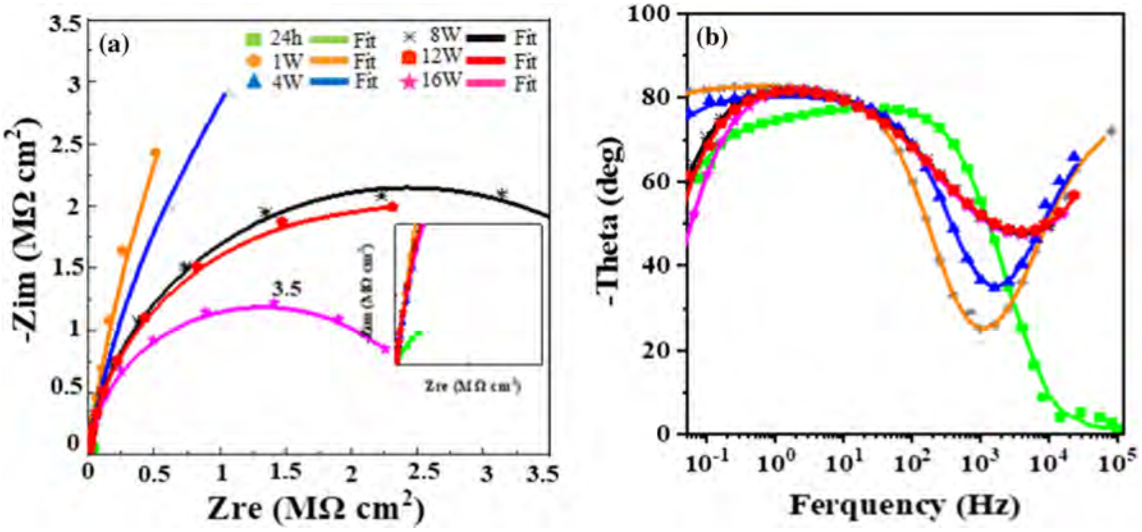

Figure 15 **a** Nyquist and **b** bode-phase plots of OX2 in PBS solution at pH 7.4 during immersion for 16 weeks. lines and symbols represent the fitted and experimental data, respectively.

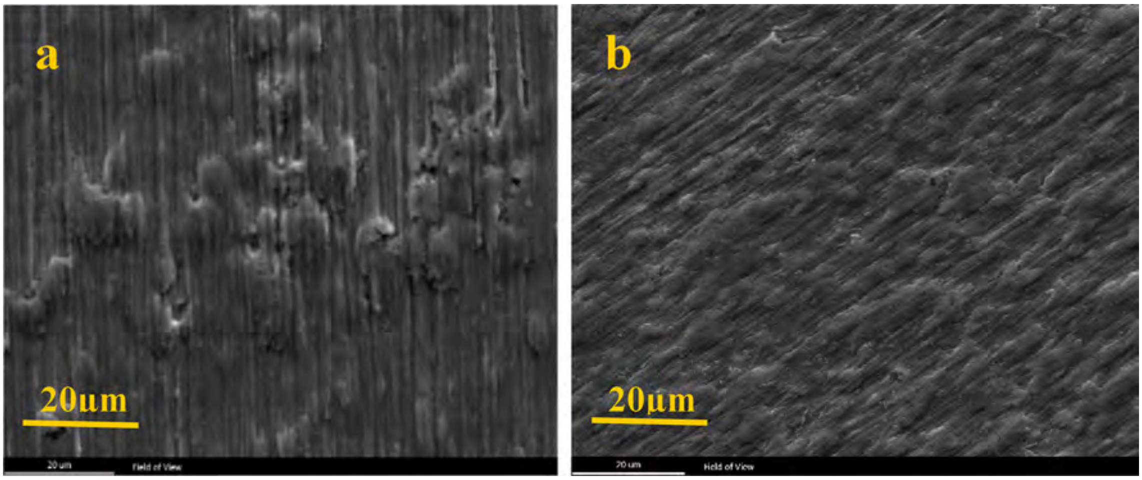

Figure 16 SEM images of OX2 after immersion in PBS for **a** 24 h and **b** 16 weeks.

16 weeks is still big enough to reveal a complete barrier in PBS.

It may be attributed to the stable oxide coating consisting of *m*-ZrO_2 and *t*-ZrO_2 phases which block the electrolyte from penetrating the vulnerable region (coating) consequently elevating the resistance [54]. The microstructure and surface morphology, phase composition, and thickness of the coating are important factors that affect corrosion performance. While phase composition effects in the short term, the thickness and porosity are affecting factors in the long term [55]. As mentioned previously, in the OX2 specimen, the ZrO_2 coating with the compact barrier layer with higher relative density and less porosity are beneficial to corrosion resistance. It is concluded that although the coating thickness may be effective in determining corrosion performance, porosity and surface morphology may have an essential role. The corrosion attack can occur when the substrate is exposed to the penetrated aggressive solution, which shows an additional capacitive loop. Considering Fig. 16a, no corrosion attack and corrosion product were observed even after 16 weeks of immersion in PBS due to the high protection offered by ZrO_2 coating. The surface morphology of the OX2 specimen after immersion for 24 h and 16 weeks is shown in Fig. 16. No holes are observed in the coating surface thus which confirms the lack of significant corrosion attack or notable degradation of the oxide layer compared to the pristine surface morphology

(Fig. 2b) indicating high stability in the solution. Additionally, the pores on the coating surface are relatively small and able to limit diffusion of the corrosion medium [56]. The high corrosion and tribocorrosion resistance of the OX2 specimen bode well for orthopedic implants such as knee joints.

Conclusions

Thermal oxidation was performed on the Zr–2.5Nb alloy in the air at different operating.

temperatures and times. The following conclusions are.

1. The black oxide layers prepared at 523 °C were compact regardless of oxidation time and had the suitable thickness and roughness for biomedical applications.
2. The resultant microcrystalline zirconium oxide layer in all specimens was composed of monoclinic and tetragonal phases and had high adhesion to the substrate.
3. The thickness of the oxide coating increased significantly at higher temperatures but beyond 700 °C, the coating became white and delaminated from the substrate.
4. The maximum value of micro and nanohardness and elastic modulus were obtained for the oxide layer prepared at 523 °C for 4 h.
5. Tribocorrosion tests revealed that no decrease occurred in the potential during sliding in PBS for OX2 and OX3 coatings, especially those formed at a lower temperature. This means that the wear scar did not penetrate the coating to reach the substrate confirming the high scratch resistance.
6. The smallest volume loss in the tribocorrosion test was achieved for the specimen treated for 4 h at 523 °C. This can be attributed to the largest H/E ratio in which delamination was the major wear mechanism.
7. Thermal oxidation at 523 °C for 4 h also increased the corrosion resistance and according to long-term electrochemical impedance test results, the corrosion resistance was still high even after 16 weeks of immersion in PBS.

Author contributions

FS: Conceptualization, Investigation, Data curation, Formal analysis, Methodology, Validation, Visualization, Resources, Writing-original draft preparation. KR: Conceptualization, Methodology, Project administration, Supervision, Validation, Visualization, Review and Editing. MHE: Conceptualization, Methodology, Project administration, Supervision, Validation, Visualization, Review and Editing. HRS: Conceptualization, Supervision, Validation, Visualization, Review and Editing. PKC: Methodology, Review and Editing.

Funding

This research did not receive any specific grant from funding agencies in the public, commercial, or not-for-profit sectors.

Declarations

Conflict of interest The authors declare that they have no known competing financial interests or personal. Relationships that could have appeared to influence the work reported in this paper. The authors declare that they have no conflict of interest.

References

[1] Kozakiewicz M, Gmyrek T, Zajdel R, Konieczny B (2021) Custom-made zirconium dioxide implants for craniofacial bone reconstruction. Materials (Basel) 14:1–20. https://doi.org/10.3390/ma14040840

[2] Xiang S, Zhao Y, Li Z et al (2019) Clinical outcomes of ceramic femoral prosthesis in total knee arthroplasty: a systematic review 11 medical and health sciences 1103 clinical sciences. J Orthop Surg Res 14:1–10. https://doi.org/10.1186/s13018-019-1090-4

[3] Ji HM, Ha YC, Baek JH, Ko YB (2015) Advantage of minimal anterior knee pain and long-term survivorship of cemented single radius posterior-stabilized total knee arthroplasty without patella resurfacing. Clin Orthop Surg 7:54–61. https://doi.org/10.4055/CIOS.2015.7.1.54

[4] Bordini B, Ancarani C, Fitch DA (2016) Long-term survivorship of a medial-pivot total knee system compared with

other cemented designs in an arthroplasty registry. J Orthop Surg Res 11:44. https://doi.org/10.1186/S13018-016-0388-8

[5] Patil NA, Kandasubramanian B (2020) Biological and mechanical enhancement of zirconium dioxide for medical applications. Ceram Int 46:4041–4057. https://doi.org/10.1016/j.ceramint.2019.10.220

[6] Kunrath MF, Gupta S, Lorusso F et al (2021) Oral tissue interactions and cellular response to zirconia implant-prosthetic components: a critical review. Materials (Basel) 14:1–24. https://doi.org/10.3390/ma14112825

[7] Ispas A, Iosif L, Murariu- Măgureanu C, Craciun A (2021) Zirconia in dental medicine : a brief overview of its properties and processing techniques. Hum Vet Med Cluj-Napoca 13:33–39

[8] Wu J, Lu P, Dong L et al (2020) Combination of plasma electrolytic oxidation and pulsed laser deposition for preparation of corrosion-resisting composite film on zirconium alloys. Mater Lett 262:127080. https://doi.org/10.1016/j.matlet.2019.127080

[9] Zhu Y, Liu K, Deng J, Ye J, Ai F, Ouyang H, Tianlong W, Jia J, Cheng Xigao, Wang X (2019) 3D printed zirconia ceramic hip joint with precise structure and broad-spectrum antibacterial properties. Int J Nanomed 14:5977–5987. https://doi.org/10.2147/IJN.S202457

[10] Kunčická L, Kocich R, Lowe TC (2017) Advances in metals and alloys for joint replacement. Prog Mater Sci 88:232–280. https://doi.org/10.1016/j.pmatsci.2017.04.002

[11] Farhan Zaludin MA, Zahid Jamal ZA, Derman MN, Kasmuin MZ (2019) Corrosion analysis of hydroxyapatite coated magnesium in simulated body fluid (SBF), phosphate buffered saline (PBS), and ringer's solution. Mater Today Proc 16:1686–1691. https://doi.org/10.1016/j.matpr.2019.06.037

[12] Afzal A (2014) Implantable zirconia bioceramics for bone repair and replacement: a chronological review. Mater Express 4:1–12. https://doi.org/10.1166/MEX.2014.1148

[13] Fook P, Riemer O (2019) Characterization of zirconia-based ceramics after microgrinding. J Micro Nano-Manuf 7:1–5. https://doi.org/10.1115/1.4043693

[14] Malinovschi V, Marin A, Negrea D, Andrei V, Coaca E (2017) Tetragonal ZrO_2 phase stabilization in coating layers prepared on Zr–2.5%Nb alloy during plasma electrolytic oxidation in sodium aluminate electrolytes. Mater Res Express 4(9):095702. https://doi.org/10.1088/2053-1591/aa87c9

[15] Tsukamoto R, Pezzotti G, Ogino M et al (2006) Zirconia Knee Wear and Raman Spectroscopy Studies Compares 3.5-Mrad and 7-Mrad UHMWPE Inserts. Key Eng Mater 309–311:1285–1288. https://doi.org/10.4028/www.scientific.net/kem.309-311.1285

[16] Ling Y, Li Q, Zheng H et al (2021) Optimisation on the stability of CaO-doped partially stabilised zirconia by microwave heating. Ceram Int 47:8067–8074. https://doi.org/10.1016/j.ceramint.2020.11.161

[17] Huang W, Qiu H, Zhang Y et al (2022) Microstructure and phase transformation behavior of Al_2O_3–ZrO_2 under microwave sintering. Ceram Int. https://doi.org/10.1016/J.CERAMINT.2022.09.376

[18] Amat NF, Muchtar A, Amril MS et al (2019) Effect of sintering temperature on the aging resistance and mechanical properties of monolithic zirconia. J Mater Res Technol 8:1092–1101. https://doi.org/10.1016/J.JMRT.2018.07.017

[19] Ezzet KA, Hermida JC, Colwell CW, D'Lima DD (2004) Oxidized zirconium femoral components reduce polyethylene wear in a knee wear simulator. Clin Orthop Relat Res 428:120–124. https://doi.org/10.1097/01.BLO.0000148576.70780.13

[20] Gautam A, Gautam C, Mishra M et al (2021) Synthesis, structural, mechanical, and biological properties of Hap–ZrO2–hBN biocomposites for bone regeneration applications. Ceram Int 47:30203–30220. https://doi.org/10.1016/j.ceramint.2021.07.200

[21] Zhou FY, Wang BL, Qiu KJ et al (2012) Microstructure, corrosion behavior and cytotoxicity of Zr–Nb alloys for biomedical application. Mater Sci Eng C 32:851–857. https://doi.org/10.1016/j.msec.2012.02.002

[22] Ries MD (2006) Oxidized zirconium in total joint arthroplasty. Semin Arthroplast JSES 17:161–164. https://doi.org/10.1053/j.sart.2006.09.011

[23] Heilig ML (1994) United states patent office. ACM SIGGRAPH Comput Graph 28:131–134. https://doi.org/10.1145/178951.178972

[24] Hobbs LW, Rosen VB, Mangin SP et al (2005) Oxidation microstructures and interfaces in the oxidized zirconium knee. Int J Appl Ceram Technol 2:221–246. https://doi.org/10.1111/j.1744-7402.2005.02025.x

[25] Sandhyarani M, Ashfaq M, Arunnellaiappan T et al (2015) Effect of electrical parameters on morphology and in-vitro corrosion resistance of plasma electrolytic oxidized films formed on zirconium. Surf Coat Technol 269:286–294. https://doi.org/10.1016/J.SURFCOAT.2015.03.001

[26] Borik MA, Bredikhin SI, Bublik VT et al (2017) The impact of structural changes in ZrO_2–Y_2O_3 solid solution crystals grown by directional crystallization of the melt on their transport characteristics. Mater Lett 205:186–189. https://doi.org/10.1016/j.matlet.2017.06.059

[27] Wang X, Wu G, Zhou B, Shen J (2012) Improvement on laser-induced damage threshold of sol-gel ZrO_2 coatings by crystal structure tuning. Opt Express 20:186–189. https://doi.org/10.1364/oe.20.024482

[28] Arantes TM, Mambrini GP, Stroppa DG et al (2010) Stable colloidal suspensions of nanostructured zirconium oxide synthesized by hydrothermal process. J Nanoparticle Res 12:3105–3110. https://doi.org/10.1007/s11051-010-9906-5

[29] Bhaskar S, Awin EW, Kumar KCH et al (2020) Design of nanoscaled heterojunctions in precursor-derived *t*-ZrO_2/SiOC(N) nanocomposites: Transgressing the boundaries of catalytic activity from UV to visible light. Sci Rep 10:1–13. https://doi.org/10.1038/s41598-019-57394-8

[30] Cao D, Cai W, Tao W et al (2017) Lactic acid production from glucose over a novel Nb_2O_5 nanorod catalyst. Catal Lett 147:926–933. https://doi.org/10.1007/s10562-017-1988-6

[31] Hoomehr B, Raeissi K, Ashrafizadeh F et al (2021) Electrophoretic deposition of bioactive glass/zirconia core-shell nanoparticles on Ti_6Al_4V substrate. Ceram Int 47:34959–34969. https://doi.org/10.1016/j.ceramint.2021.09.037

[32] Hunter G, Jones WM, Spector M (2005) Oxidized zirconium. Total Knee Arthroplast Guid Get Better Perform. https://doi.org/10.1007/3-540-27658-0_59

[33] Sourani F, Enayati MH, Taghipour M (2021) High-Temperature Oxidation and Wear Behavior of (Fe, Cr)Al Intermetallic Compound and (Fe, Cr)Al-Al2O3 Nanocomposites. J Mater Eng Perform 30:34959–34969. https://doi.org/10.1007/s11665-021-05710-7

[34] Koneska Z, Manojlović R, Stoevska-Gogovska D (2017) Air-thermal oxidation of zirconium. J Eng Process Manag 1:81–85. https://doi.org/10.7251/jepm1709081k

[35] Nakonieczny DS, Sambok A, Antonowicz M, Basiaga M, Paszenda ZK, Krawczyk C, Ziębowicz B, Lemcke H, Kałużyński Piotr (2019) Ageing of zirconia dedicated to dental prostheses for bruxers part 2: influence of heat treatment for surface morphology, phase composition and mechanical properties. Rev Adv Mat Sci 58(1):218–225. https://doi.org/10.1515/rams-2019-0027

[36] Cao C, Ford D, Bishnoi S et al (2013) Detection of surface carbon and hydrocarbons in hot spot regions of niobium superconducting rf cavities by Raman spectroscopy. Phys Rev Spec Top Accel Beams. https://doi.org/10.1103/PhysRevSTAB.16.064701

[37] Bressan JD, Tramontin A, Rosa C (2005) Modeling of nanoindentation of bulk and thin film by finite element method. Wear 258:115–122. https://doi.org/10.1016/J.WEAR.2004.05.021

[38] Yoda I, Koseki H, Tomita M et al (2014) Effect of surface roughness of biomaterials on staphylococcus epidermidis adhesion. BMC Microbiol 14:1–7. https://doi.org/10.1186/s12866-014-0234-2

[39] Abbass SJ, Abed RI (2021) Mechanical analysis of hip & knee implants regarding different activities conditions and different materials. Mater Today Proc 42:2193–2201. https://doi.org/10.1016/j.matpr.2020.12.304

[40] Heyse TJ, Haas SB, Efe T (2012) The use of oxidized zirconium alloy in knee arthroplasty. Exp Rev Med Devices 9:409–421. https://doi.org/10.1586/erd.12.30

[41] Rieker CB (2004) Is the OXINIUM technology a useful technology in total joint arthroplasty? Bioceram Jt Arthroplast. https://doi.org/10.1007/978-3-7985-1968-8_18

[42] Qin W, Nam C, Li HL, Szpunar JA (2007) Tetragonal phase stability in ZrO_2 film formed on zirconium alloys and its effects on corrosion resistance. Acta Mater 55:112–117. https://doi.org/10.1016/j.actamat.2006.10.030

[43] Daniel Barros M, Hotza D, Janssen R (2021) Dopant diffusion at the interface of TiO_2-MnO-doped alumina/alumina layers in sintered laminates. Int J Ceram Eng Sci 3:105–112. https://doi.org/10.1002/ces2.10090

[44] Sato H, Yamada K, Pezzotti G et al (2008) Mechanical properties of dental zirconia ceramics changed with sandblasting and heat treatment. Dent Mater J 27:408–414. https://doi.org/10.4012/DMJ.27.408

[45] Ghafaripoor M, Raeissi K, Santamaria M, Hakimizad A (2018) Surface & Coatings Technology The corrosion and tribocorrosion resistance of PEO composite coatings containing α-Al_2O_3 particles on 7075 Al alloy. Surf Coat Technol 349:470–479. https://doi.org/10.1016/j.surfcoat.2018.06.027

[46] Akbari E, Di Franco F, Ceraolo P et al (2018) Electrochemically-induced TiO_2 incorporation for enhancing corrosion and tribocorrosion resistance of PEO coating on 7075 Al alloy. Corros Sci 143:314–328. https://doi.org/10.1016/j.corsci.2018.08.037

[47] Malayoğlu U, Tekin KC, Malayoğlu U, Belevi M (2020) Mechanical and electrochemical properties of PEO coatings on zirconium alloy. Surf Eng 36:800–808. https://doi.org/10.1080/02670844.2019.1706233

[48] Zhang C, Wang W, Xing W, Liu L (2020) Understanding on toughening mechanism of bioinspired bulk metallic glassy composites by thermal spray additive manufacturing. Scr Mater 177:112–117. https://doi.org/10.1016/j.scriptamat.2019.10.017

[49] Malinovschi V, Marin A, Negrea D, Andrei V, Coaca E (2017) Tetragonal ZrO_2 phase stabilization in coating layers prepared on Zr–2.5%Nb alloy during plasma electrolytic oxidation in sodium aluminate electrolytes. Mater Res Express 4(9):095702. https://doi.org/10.1088/2053-1591/aa87c9

[50] Shan L, Wang Y, Li J et al (2013) Tribological behaviours of PVD TiN and TiCN coatings in artificial seawater. Surf Coat

Technol 226:40–50. https://doi.org/10.1016/j.surfcoat.2013.03.034

[51] Sowa M, Simka W (2018) Effect of DC plasma electrolytic oxidation on surface characteristics and corrosion resistance of zirconium. Materials (Basel) 11:9–12. https://doi.org/10.3390/ma11050723

[52] Zhang Y, Chen F, Zhang Y, Du C (2020) 1Influence of graphene oxide additive on the tribological and electrochemical corrosion properties of a PEO coating prepared on AZ31 magnesium alloy. Tribol Int 146:106135. https://doi.org/10.1016/J.TRIBOINT.2019.106135

[53] Kaliaraj GS, Vishwakarma V, Alagarsamy K, Kamalan Kirubaharan AM (2018) Biological and corrosion behavior of *m*-ZrO_2 and *t*-ZrO_2 coated 316L SS for potential biomedical applications. Ceram Int 44:116–122. https://doi.org/10.1016/j.ceramint.2018.05.103

[54] Hoomehr B, Raeissi K, Ashrafizadeh F et al (2022) Corrosion performance and biological properties of electrophoretically deposited bioactive glass-zirconia core-shell composite coating on Ti6Al4V substrate. Surf Coat Technol 434:128209. https://doi.org/10.1016/j.surfcoat.2022.128209

[55] Chen Y, Nie X, Northwood DO (2010) Investigation of plasma electrolytic oxidation (PEO) coatings on a Zr–2.5Nb alloy using high temperature/pressure autoclave and tribological tests. Surf Coat Technol 205:1774–1782. https://doi.org/10.1016/j.surfcoat.2010.08.038

[56] Hussein RO, Northwood DO, Su JF, Nie X (2013) A study of the interactive effects of hybrid current modes on the tribological properties of a PEO (plasma electrolytic oxidation) coated AM60B Mg-alloy. Surf Coatings Technol 215:421–430. https://doi.org/10.1016/J.SURFCOAT.2012.08.082